

Beam Charge Effect on the Beam Spin Asymmetry associated with Deeply Virtual Compton Scattering on the Proton

Xianguo Lu*

Physics Department, Peking University, Beijing, 100871

December 4, 2006

Abstract

Theoretical calculations reveal that the Beam Spin Asymmetry (BSA) $A_{LU}(\phi)$ associated with Deeply Virtual Compton Scattering (DVCS) on the nucleon depends on the beam charge, and that for the $\sin\phi$ moments obtained with electron and positron beams at the HERMES kinematics holds: a) $-A_{LU}^{\sin\phi,e^+} = A_{LU}^{\sin\phi,e^-}$, if power-suppressed terms are neglected; b) $|A_{LU}^{\sin\phi,e^+}| \neq |A_{LU}^{\sin\phi,e^-}|$, including power-suppressed terms.

Measurements of the BSA with a positron beam have been performed at HERMES. In this report, the first look at the BSA with an electron beam on the proton is described. The results are $A_{LU}^{\sin\phi,e^-} = 0.26 \pm 0.06(stat.)$, $A_{LU}^{\sin 2\phi,e^-} = 0.06 \pm 0.06(stat.)$. They are compared to the BSA with a positron beam and $-A_{LU}^{\sin\phi,e^+} \simeq A_{LU}^{\sin\phi,e^-}$ is observed within statistical uncertainties.

Contents

1	Introduction	4
1.1	Beam Spin Asymmetry Associated with DVCS with e^\pm Beams . . .	4
1.2	Kinematics	7
1.3	BSA Measurement at the HERMES Experiment	9

*Email: xianguo.lu@desy.de

1.3.1	Beams and Targets	9
1.3.2	Detection of the Particles in the Final State	10
2	Data Analysis	11
2.1	Events Selection	11
2.1.1	Data Quality Cuts	12
2.1.2	DIS Events Selection	12
2.1.3	Exclusive Events Selection	12
2.1.4	Discussion	12
2.2	BSA Extraction	13
2.2.1	Binned Least Square Fit	13
2.2.2	Unbinned Maximum Likelihood Fit	13
3	Results and Conclusion	14
3.1	Data Statistics	14
3.2	BSAs with e^\pm Beams	14
3.3	Kinematic Dependence of the BSAs with e^\pm Beams	15
3.4	Conclusion	15

List of Figures

1	Diagrams for the exclusive electroproduction of a real photon off a proton. (a) DVCS process. (b) BH process. The two processes have identical final states. e (e'), P (P'), and γ^* (γ) are the incoming (outgoing) electron, initial (final) proton and virtual (real) photon respectively.	4
2	Kinematics of the DVCS process. The production plane denotes the one in which γ^* and γ are emitted, and the scattering plane the one where the lepton is scattered.	7
3	The HERMES spectrometer. Tracking system (red parts): Drift Vertex Chamber (DVC), Front Chamber (FC1/2), Magnet Chambers (MC1-3) and Back Chamber (BC1/2,BC3/4). Particle identification (PID) system (green parts): Ring-Imaging Čerenkov-counter (RICH), Transition Radiation Detector (TRD), Pre-shower detector (H2), and Calorimeter.	9
4	Kinematic distributions of the DIS events, normalized per DIS event. At the limits of ν and W^2 , differences between the distributions from the two data productions are pronounced. $N_{DIS}^{00d0,unpol.} = 5,092,595$, $N_{DIS}^{05b1,pol.+unpol.} = 3,619,532$	17
5	Kinematic distributions of the exclusive events, normalized per 1000 DIS events. $N_{Exclusive}^{00d0,unpol.} = 7,784$, $N_{Exclusive}^{05b1,pol.+unpol.} = 5,742$	18

6	Kinematic distributions of the exclusive events, normalized per 1000 DIS events. The average values for the 00d0/05b1 production are: $\langle x_{Bj} \rangle = 0.10 / 0.09$, $\langle y \rangle = 0.51 / 0.51$, $\langle Q^2 \rangle = 2.5 / 2.4 \text{ GeV}^2$, $\langle W^2 \rangle = 24.6 / 24.8 \text{ GeV}^2$	19
7	Kinematic distributions of the DIS events, normalized per DIS event. For the distributions from the 00d0 unpolarized and 05b1 polarized data, greater differences are observed at kinematic limits.	20
8	BSAs with e^\pm beams by the least square fit to different functions. The results indicate that whether the fitting function has a constant term does not have critical influence on the extraction of $A_{LU}^{\sin \phi}$ and $A_{LU}^{\sin 2\phi}$	21
9	BSAs with e^\pm beams by different fits to a function without constant term. Results by different methods are compatible. The points calculated by Eqs. (32) and (33) and the dash lines by the least square fit to the points are for the comparison with the adopted results by the unbinned maximum likelihood method (solid lines).	22
10	Kinematic dependence of the BSAs with e^\pm beams. The BSAs with an e^+ beam in the bottom figure is scaled by -1. The black and red dashed lines correspond to the average results with e^- and e^+ beams respectively.	23

List of Tables

1	Summary for the average beam polarizations, event numbers, and the average kinematics of the exclusive events.	14
2	Results on BSAs for two different beam charges, obtained by the method of maximum likelihood.	15

1 Introduction

Deeply virtual Compton scattering (DVCS) is hard photoproduction of a real photon, i.e., $\gamma^* N \rightarrow \gamma N'$, where $N(N')$ is a nucleon. Its interference with the Bethe-Heitler (BH) process leads to a beam spin asymmetry (BSA), which is charge-dependent according to theoretical calculations. A beam spin asymmetry, which is charge independent, arises also in the DVCS process alone. These two asymmetries contribute together to the asymmetries observed experimentally. The motivation of this analysis is to extract the BSA with positron/electron beams from the HERMES 2000/2005 data production and to compare the results with the theoretical predictions.

1.1 Beam Spin Asymmetry Associated with DVCS with e^\pm Beams

In exclusive leptonproduction of a real photon off a nucleon

$$l(k) + N(p) \rightarrow l(k') + N(p') + \gamma(q'), \quad (1)$$

where k, k', p, p' and q' denote the four-momenta of the corresponding particles, a real photon can be produced via hard photoproduction, i.e., the DVCS process: a virtual photon is emitted by the incoming lepton¹ and interacts with a parton in the nucleon, followed by emission of a real photon [Figure 1(a)]. The real photon can also be emitted by the incoming or outgoing lepton in the BH process [Figure 1(b)]. The two processes have identical final states, and thus they are experimentally indistinguishable and their amplitudes add coherently.

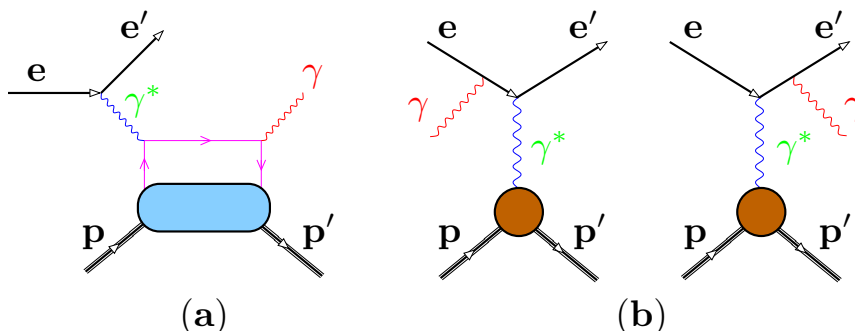


Figure 1: Diagrams for the exclusive electroproduction of a real photon off a proton. (a) DVCS process. (b) BH process. The two processes have identical final states. e (e'), P (P'), and γ^* (γ) are the incoming (outgoing) electron, initial (final) proton and virtual (real) photon respectively.

¹In this report a lepton refers to an electron or a positron.

For an unpolarized target, the four-fold cross section for Process (1) is given by [1]

$$\frac{d\sigma}{dx_{Bj}dyd|t|d\phi} = \frac{\alpha_{em}^3 x_{Bj}y}{8\pi Q^2 \sqrt{1+\epsilon^2}} \left| \frac{\tau}{e^3} \right|^2, \quad (2)$$

with the fine structure constant α_{em} , the lepton charge e and

$$\epsilon \equiv 2x_{Bj} \frac{M_N}{Q}. \quad (3)$$

This cross section depends on the Bjorken variable x_{Bj} , the lepton energy fraction y , the squared 4-momentum transfer to the nucleon t , the azimuthal angle ϕ , the photon virtuality Q and the nucleon mass M_N (cf. Section 1.2).

The amplitude τ is given by the coherent sum of the DVCS amplitude τ_{DVCS} and the BH amplitude τ_{BH} . Thus

$$|\tau|^2 = |\tau_{BH}|^2 + |\tau_{DVCS}|^2 + \underbrace{\tau_{DVCS}\tau_{BH}^* + \tau_{DVCS}^*\tau_{BH}}_{\mathcal{I}}, \quad (4)$$

where \mathcal{I} denotes the interference term. For a longitudinally polarized beam of helicity λ , the three terms on the right hand side of Eq. (4) can be expanded in a Fourier series in ϕ to the twist-three approximation [1]:

$$|\tau_{BH}|^2 = \frac{e^6}{x_{Bj}^2 y^2 (1+\epsilon^2)^2 t P_1(\phi) P_2(\phi)} (c_0^{BH} + \sum_{n=1}^2 c_n^{BH} \cos n\phi), \quad (5)$$

$$|\tau_{DVCS}|^2 = \frac{e^6}{y^2 Q^2} (c_0^{DVCS} + \sum_{n=1}^2 c_n^{DVCS} \cos n\phi + \lambda s_1^{DVCS} \sin \phi), \quad (6)$$

$$\begin{aligned} \mathcal{I} &= \frac{-\eta e^6}{x_{Bj} y^3 P_1(\phi) P_2(\phi) t} \\ &\times (c_0^{\mathcal{I}} + \sum_{n=1}^3 c_n^{\mathcal{I}} \cos n\phi + \lambda \sum_{n=1}^2 s_n^{\mathcal{I}} \sin n\phi), \end{aligned} \quad (7)$$

where $\eta = \pm 1$ corresponds to the sign of the beam charge and $P_{1,2}(\phi)$ are defined in the lepton BH propagators:

$$Q^2 P_1 \equiv (k - q')^2, \quad (8)$$

$$Q^2 P_2 \equiv [k - (p' - p)]^2. \quad (9)$$

Note that the helicity-dependence of Eqs. (5)-(7) is explicitly illustrated by λ which is extracted from the original expressions of the Fourier coefficients c_n and s_n in reference [1].

The coefficients $c_{0,n}^{BH}$ can be expressed solely in terms of the Dirac and Pauli form factors of the nucleon; $c_{0,n}^{DVCS,\mathcal{I}}$ and $s_n^{DVCS,\mathcal{I}}$ depend on the Compton form

factors (CFFs) which can be given in terms of the generalized parton distributions (GPDs) [1]. The latter provide access to the total angular momentum of the quarks in the nucleon [2, 3].

The beam spin asymmetry (BSA) is defined in measurements of Process (1) with longitudinally (L) polarized beams of opposite polarizations (\rightleftharpoons for $\lambda = \pm 1$) and unpolarized (U) targets:

$$A_{LU}(\phi) = \frac{d\sigma^{\rightarrow} - d\sigma^{\leftarrow}}{d\sigma^{\rightarrow} + d\sigma^{\leftarrow}}. \quad (10)$$

It can also be defined equivalently and more generally:

$$d\sigma_{LU}(\phi) = d\sigma_{UU}(\phi)[1 + \lambda A_{LU}(\phi)], \quad (11)$$

in which UU stands for unpolarized beams and targets.

With fixed x_{Bj} , Q^2 and t , $A_{LU}(\phi)$ reads [cf. Eqs. (5)-(7)]

$$A_{LU}(\phi) = \frac{\frac{s_1^{DVCS} \sin \phi}{Q^2} - \eta \frac{s_1^{\mathcal{I}} \sin \phi + s_2^{\mathcal{I}} \sin 2\phi}{x_{Bj} y P_1(\phi) P_2(\phi) t}}{\frac{c_0^{BH} + \sum_{n=1}^2 c_n^{BH} \cos n\phi}{x_{Bj}^2 (1+\epsilon^2)^2 t P_1(\phi) P_2(\phi)} + \frac{c_0^{DVCS} + \sum_{n=1}^2 c_n^{DVCS} \cos n\phi}{Q^2} - \eta \frac{c_0^{\mathcal{I}} + \sum_{n=1}^3 c_n^{\mathcal{I}} \cos n\phi}{x_{Bj} y P_1(\phi) P_2(\phi) t}}, \quad (12)$$

where, at the HERMES average kinematics, the BH part prevails in the denominator [1] with c_0^{BH} dominating over $c_{1,2}^{BH}$. And $s_1^{\mathcal{I}}$ arises from the twist-two level while $s_2^{\mathcal{I}}$ and s_1^{DVCS} from the twist-three and therefore are suppressed [1]. As a result, the BH propagators almost cancel. Such approximation can be illustrated as:

$$A_{LU}(\phi) \stackrel{HERMES}{\approx} \frac{\frac{s_1^{DVCS} \sin \phi}{Q^2} - \eta \frac{s_1^{\mathcal{I}} \sin \phi + s_2^{\mathcal{I}} \sin 2\phi}{x_{Bj} y P_1(\phi) P_2(\phi) t}}{\frac{c_0^{BH} + \sum_{n=1}^2 c_n^{BH} \cos n\phi}{x_{Bj}^2 (1+\epsilon^2)^2 t P_1(\phi) P_2(\phi)}} \quad (13)$$

$$\stackrel{P.S.}{\approx} \frac{-\eta \frac{s_1^{\mathcal{I}} \sin \phi}{x_{Bj} y P_1(\phi) P_2(\phi) t}}{\frac{c_0^{BH}}{x_{Bj}^2 (1+\epsilon^2)^2 t P_1(\phi) P_2(\phi)}} \quad (14)$$

$$= -\eta (1 + \epsilon^2)^2 \frac{x_{Bj}}{y} \frac{s_1^{\mathcal{I}}}{c_0^{BH}} \sin \phi. \quad (15)$$

where $P.S.$ is short for Power-Suppression. Because ϵ is a small number at HERMES kinematics ²,

$$A_{LU}(\phi) \approx -\eta \frac{x_{Bj}}{y} \frac{s_1^{\mathcal{I}}}{c_0^{BH}} \sin \phi. \quad (16)$$

$A_{LU}(\phi)$ can be parameterized as

$$A_{LU}(\phi) = A_{LU}^{\sin \phi} \sin \phi + A_{LU}^{\sin 2\phi} \sin 2\phi. \quad (17)$$

²In this analysis, $\epsilon > \sim 0.1$.

where the factors are ϕ -independent.

On the one hand, at the HERMES kinematics, when power-suppressed terms are neglected, A_{LU} is proportional to the beam charge [Eqs. (13)-(16)]. Thus we expect

$$-A_{LU}^{sin\phi, e^+} = A_{LU}^{sin\phi, e^-}. \quad (18)$$

On the other hand, A_{LU} , both in the denominator and numerator, is a mixture of beam-charge dependent interference and beam-charge independent DVCS effects [Eqs. (12)]. If power-suppressed terms are not neglected, we have

$$|A_{LU}^{sin\phi, e^+}| \neq |A_{LU}^{sin\phi, e^-}|. \quad (19)$$

1.2 Kinematics

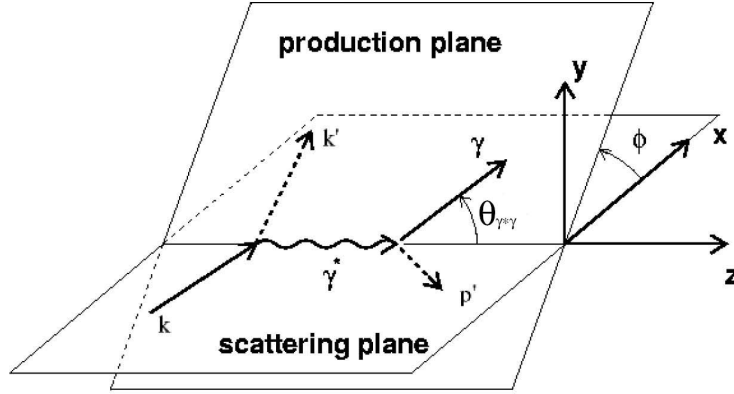


Figure 2: Kinematics of the DVCS process. The production plane denotes the one in which γ^* and γ are emitted, and the scattering plane the one where the lepton is scattered.

In order to describe Process (1), the following kinematic variables are defined, assuming a fixed target in the lab frame:

- The azimuthal angle—the angle between the production plane and the scattering plane (Figure 2)

$$\phi \equiv \arccos \frac{\vec{q} \times \vec{k}' \cdot \vec{q} \times \vec{q}'}{|\vec{q} \times \vec{k}'| |\vec{q} \times \vec{q}'|} \cdot \frac{\vec{q}' \cdot \vec{q} \times \vec{k}'}{|\vec{q}' \cdot \vec{q} \times \vec{k}'|}. \quad (20)$$

- The photon virtuality

$$Q^2 \equiv -q^2 = -(k - k')^2 \stackrel{lab}{\approx} 4EE' \sin^2 \frac{\theta}{2}, \quad (21)$$

in which q denotes the 4-momentum transfer by the virtual photon, θ the scattering angle of the lepton, and E (E') the energy of the incoming (outgoing) lepton in the lab frame.

- The energy of the virtual photon in the lab frame

$$\nu \equiv \frac{pq}{M_N} \stackrel{lab}{=} E - E', \quad (22)$$

where M_N is the nucleon mass, which is the proton rest mass M_P in the case of a proton target.

- The lepton energy fraction in the lab frame

$$y = \frac{pq}{pk} \stackrel{lab}{=} \frac{\nu}{E}. \quad (23)$$

- The squared invariant mass of the $\gamma^* - N$ system

$$W^2 \equiv (q + p)^2 = M_N^2 + 2M_N\nu - Q^2. \quad (24)$$

- The Bjorken variable x_{Bj}

$$x_{Bj} \equiv \frac{Q^2}{2pq} = \frac{Q^2}{2M_N\nu}. \quad (25)$$

- The missing mass squared for the recoiling proton

$$M_x^2 \equiv (q + p - q')^2. \quad (26)$$

- The polar angle between the virtual and real photons

$$\theta_{\gamma^*\gamma} \equiv \arccos \frac{\vec{q} \cdot \vec{q}'}{|\vec{q}||\vec{q}'|}. \quad (27)$$

- The squared 4-momentum transfer between incoming and outgoing nucleon

$$t \equiv (p' - p)^2 = (q - q')^2. \quad (28)$$

In the process $e + p \rightarrow e' + p' + \gamma$, i.e. if the target nucleon stays intact, it can be expressed as the "constrained" momentum transfer

$$\begin{aligned} t_c &\equiv t(M_x^2 = M_p^2) \\ &= \frac{-Q^2 - 2\nu(\nu - \sqrt{\nu^2 + Q^2} \cos \theta_{\gamma^*\gamma})}{1 + \frac{1}{M_P}(\nu - \sqrt{\nu^2 + Q^2} \cos \theta_{\gamma^*\gamma})}. \end{aligned} \quad (29)$$

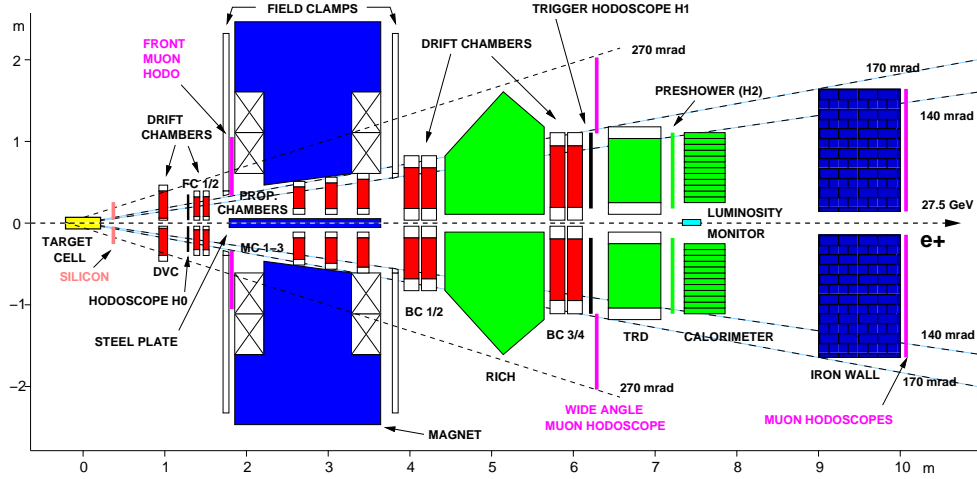


Figure 3: The HERMES spectrometer. Tracking system (red parts): Drift Vertex Chamber (DVC), Front Chamber (FC1/2), Magnet Chambers (MC1-3) and Back Chamber (BC1/2, BC3/4). Particle identification (PID) system (green parts): Ring-Imaging Čerenkov-counter (RICH), Transition Radiation Detector (TRD), Pre-shower detector (H2), and Calorimeter.

1.3 BSA Measurement at the HERMES Experiment

The HERMES experiment at the HERA storage ring at DESY is a fixed target experiment scattering longitudinally polarized electron/positron beams off polarized or unpolarized gas targets.

Because the HERMES detector (Figure 3) is a forward spectrometer [4] and the BH process dominates in the kinematic region covered by HERMES, it is difficult to extract the Fourier coefficients in $|\tau_{DVCS}|^2$ and \mathcal{I} [Eqs. (6), (7)] by cross section measurements. However the measurement of a cross section asymmetry with respect to the beam helicity, which exploits the BH/DVCS interference, provides an alternative way to access these Fourier coefficients and thus the GPDs.

Except for a short period in 1998, in 2005 and in the first half of 2006 HERA was running with electron beams. Thus at HERMES, a precise measurement of the BSA with an electron beam became possible only after the 2005 data production had been released.

1.3.1 Beams and Targets

The electron/positron beams at HERA are transversely self-polarized with a polarization of about 60% due to the net outcome of several competing effects. The Sokolov-Ternov effect [5] builds up a polarization up to a maximum of 92%, while the beam-beam interaction and non-vertical magnetic field components degrade it

to the observed level.

The transverse beam polarization is converted into a longitudinal one by the spin-rotator in front of HERMES and back to be transverse by the spin-rotator behind.

From 2002 to 2005, the target was transversely polarized. The transverse magnetic field in the target region introduces deflection to charged particles. Thus certain transverse magnet correction (TMC) methods are required to calculate the vertex and scattering angles corresponding to the case without the transverse magnetic field.

1.3.2 Detection of the Particles in the Final State

At HERMES, the detection of scattered leptons and real photons in Process (1) is mainly accomplished by the tracking and particle identification systems. For the detection of recoiling protons, a recoil detector is being commissioned.

The tracking system consists of the Drift Vertex Chamber (DVC), Front Chambers (FC1/2), Magnet Chambers (MC1-3), and the Back Chambers (BC1/2,BC3/4).

- The event vertex and scattering angles are determined by the DVC and FCs.
- The particle momenta are measured by the BCs in combination with the DVC and FCs from the track deflection by the spectrometer dipole magnets.

The particle identification system consists of the Ring-Imaging Čerenkov-counter (RICH), Transition Radiation Detector (TRD), pre-shower detector (H2) and the Calorimeter.

- The RICH, designed to separate pions, protons, and kaons, contributes to the lepton-hadron separation only for those particles with an energy below about 4 GeV. Thus in this analysis it was not used.
- The TRD exploits the fact that charged particles emit transition radiation when crossing boundaries between media with different dielectric constants. Because the energy radiated is proportional to the Lorentz factor γ of the charged particle, with the same initial energy, leptons deposit more energy than hadrons do, while the latter deposit energy through ionization only.
- The pre-shower detector is based on the fact that electromagnetic showers originating from a lepton starts usually much earlier than hadronic showers do, generating more tracks in the detector and thus more energy deposition.
- The (electromagnetic) calorimeter is of the size chosen in such a way that most of the electromagnetic showers are contained in it, but only a fraction of the hadron energy is deposited. Thus $\frac{E'}{p'} \approx 1$ holds for leptons but not for hadrons. (E' is the energy measured in the calorimeter and p' the track momentum measured by the tracking system.)

- The PID system ($PID_{2,3,5}$) provides a criterion for lepton-hadron separation. The probability of a particle being a lepton or a hadron is a function of the detector response and the particle momentum. Define

$$PID_{\mathcal{D}} = \log_{10} \frac{P_e(p, R)}{P_h(p, R)}, \quad (30)$$

where $P_{e/h}(p, R)$ is the probability of a detected particle being a lepton/hadron with momentum p and the \mathcal{D} -detector response R . And the PID system is defined as:

$$\begin{aligned} PID_2 &= PID_{\text{preshower}} + PID_{\text{calorimeter}}, \\ PID_3 &= PID_{\text{preshower}} + PID_{\text{calorimeter}} + PID_{\text{RICH}}, \\ PID_5 &= PID_{\text{TRD}}, \end{aligned} \quad (31)$$

which characterizes the relative probability of a particle being a lepton to being a hadron according to a certain combination of detectors.

In this analysis, the TRD, pre-shower, and calorimeter play an important role in the lepton-hadron separation, and the particle identification relies much on the performance of them.

Real photons are detected by the calorimeter and the energy measurement is based on the assumption that showers from leptons and real photons develop at least similarly. In fact, due to different electromagnetic shower formation probabilities for leptons and photons in the pre-shower detector, more leptons convert into showers in the pre-shower detector before reaching the calorimeter, while some photons start the conversion in the latter. As a result, the energy of these photons are overestimated.

Recoiling protons can not be detected at the present time. Thus besides the hard exclusive leptonproduction of real photons, other processes, such as exclusive π^0 -production, or semi-inclusive processes, contribute to the collected data samples. With the recoil detector, the background is supposed to be suppressed to an optimum level.

2 Data Analysis

In this analysis, two different fit techniques – Binned Least Square Fit and Unbinned Maximum Likelihood Fit – are used to extract the BSAs. After *Events Selection*, the two methods will be discussed.

2.1 Events Selection

The data samples used in this analysis were accumulated in the 2000 positron and 2005 electron runs. Unpolarized hydrogen runs from the 00d0 and 05b1 data productions were selected. To increase the statistics, transversely polarized hydrogen data from 05b1 were included as well, with an average target polarization of 0.3%.

To select the exclusive events of hard electroproduction of real photons, each event candidate was required to pass the requirements for the data quality, DIS events and exclusive events.

2.1.1 Data Quality Cuts

They can be generally summarized as the following:

- The data were marked as analyzable.
- The luminosity measurement was fine.
- The tracking system and the lepton-identification-related PID system (TRD, H2, Calorimeter) were functioning without any problem.
- The beam polarization was reasonable and the measurement was reliable.
- For the polarized target data, the target was in a reasonable state with a reasonable polarization.

2.1.2 DIS Events Selection

Besides the PID and fiducial volume cuts, the following kinematic cuts were applied:

- $W^2 > 9 \text{ GeV}^2$, $Q^2 > 1 \text{ GeV}^2$, $\nu < 22 \text{ GeV}$.

The kinematic distributions of the DIS events are shown in Figure 4.

2.1.3 Exclusive Events Selection

Each event candidate was required to have exactly one track and one untracked cluster in the calorimeter. Besides the photon fiducial volume cuts and the energy cuts, the following kinematic cuts were applied:

- $-1.5 < M_x < 1.7 \text{ GeV}$, $-t_c < 0.7 \text{ GeV}^2$, $0.03 < x_{Bj} < 0.35$, $Q^2 < 10 \text{ GeV}^2$.

The kinematic distributions of the exclusive events are shown in Figures 5 and 6.

2.1.4 Discussion

To the approximation of single photon exchange, the cross section of the DIS process is independent of the sign of the beam charge. In the kinematic region covered by HERMES, it is not expected to observe a difference between the kinematic distributions with respect to e^\pm beams.

From Figure 4 we can see that the kinematic distributions from the 00d0 and 05b1 data productions are slightly different at the limits of ν and W^2 . Separating the polarized and unpolarized parts of the 05b1 data (Figure 7), we can see that for the distributions from the 00d0 unpolarized and 05b1 polarized data, greater differences are observed at the kinematic limits, the causes of which will be investigated in systematic studies.

2.2 BSA Extraction

2.2.1 Binned Least Square Fit

In terms of event numbers, with different polarizations in both beam helicity states, Eq. (10) with positron or electron beams can be generalized as ³:

$$A_{LU}(\phi_i) = \frac{1}{\frac{1}{A'_{LU}(\phi_i)} - \frac{P^{\rightarrow} - P^{\leftarrow}}{2}}, \quad A'_{LU}(\phi_i) = \frac{1}{\frac{P^{\rightarrow} + P^{\leftarrow}}{2}} \cdot \frac{\frac{N_i^{\rightarrow}}{N_{DIS}^{\rightarrow}} - \frac{N_i^{\leftarrow}}{N_{DIS}^{\leftarrow}}}{\frac{N_i^{\rightarrow}}{N_{DIS}^{\rightarrow}} + \frac{N_i^{\leftarrow}}{N_{DIS}^{\leftarrow}}}, \quad (32)$$

with the index i meaning that the quantity is averaged (ϕ_i) or counted (N_i^{\leftrightarrow}) in the i th ϕ -bin. \rightarrow / \leftarrow stands for the positive/negative beam polarization, N/N_{DIS} the exclusive/DIS event number, and P the magnitude of the beam polarization. For the 2000 data, $P^{\rightarrow} = 54.3\%$, $P^{\leftarrow} = 55.1\%$, and for 2005, $P^{\rightarrow} = 32.4\%$, $P^{\leftarrow} = 28.6\%$.

The statistical error of $A_{LU}(\phi_i)$ is calculated according to the error propagation

$$dA_{LU}(\phi_i) = \frac{dA'_{LU}(\phi_i)}{\left[1 - \frac{P^{\rightarrow} - P^{\leftarrow}}{2} A'_{LU}(\phi_i)\right]^2}, \quad (33)$$

where $dA'_{LU}(\phi_i)$ is based on the Poisson distribution, and

$$\begin{aligned} dA'_{LU}(\phi_i) &= \frac{4}{P^{\rightarrow} + P^{\leftarrow}} \cdot \frac{N_i^{\rightarrow} N_i^{\leftarrow} N_{DIS}^{\rightarrow} N_{DIS}^{\leftarrow}}{(N_i^{\rightarrow} N_{DIS}^{\leftarrow} + N_i^{\leftarrow} N_{DIS}^{\rightarrow})^2} \sqrt{\frac{1}{N_i^{\rightarrow}} + \frac{1}{N_i^{\leftarrow}} + \frac{1}{N_{DIS}^{\rightarrow}} + \frac{1}{N_{DIS}^{\leftarrow}}} \\ &\approx \frac{4}{P^{\rightarrow} + P^{\leftarrow}} \cdot \frac{N_i^{\rightarrow} N_i^{\leftarrow} N_{DIS}^{\rightarrow} N_{DIS}^{\leftarrow}}{(N_i^{\rightarrow} N_{DIS}^{\leftarrow} + N_i^{\leftarrow} N_{DIS}^{\rightarrow})^2} \sqrt{\frac{1}{N_i^{\rightarrow}} + \frac{1}{N_i^{\leftarrow}}}. \end{aligned} \quad (34)$$

The ϕ -dependence of A_{LU} can then be extracted by fitting $A_{LU}(\phi_i)$ to $A_{LU}(\phi; \mathbf{x})$ with the least square method, where $A_{LU}(\phi; \mathbf{x}) = A_{LU}^{\sin \phi} \sin \phi + A_{LU}^{\sin 2\phi} \sin 2\phi$ with $\mathbf{x} = (A_{LU}^{\sin \phi}, A_{LU}^{\sin 2\phi})$, which is the set of unknown parameters.

2.2.2 Unbinned Maximum Likelihood Fit

From Eq. (11) we have the following probability density function:

$$f(\phi^{\leftrightarrow}) = \frac{\varepsilon(\phi^{\leftrightarrow}) \cdot d\sigma_{UU}(\phi^{\leftrightarrow}) \cdot \left[1 \pm P^{\leftrightarrow} A_{LU}(\phi^{\leftrightarrow}; \mathbf{x})\right]}{C^{\leftrightarrow}(\mathbf{x})}, \quad (35)$$

in which ϕ^{\leftrightarrow} is the measured value in each exclusive event corresponding to P^{\leftrightarrow} , $\varepsilon(\phi^{\leftrightarrow})$ is the detection efficiency, and $C(\mathbf{x})$ the normalization factor. Thus the like-

³In this analysis, $\frac{P^{\rightarrow} - P^{\leftarrow}}{2}$ and $A'_{LU}(\phi)$ are in the order of 0.01 and 0.1 respectively, thus $\frac{A'_{LU} - A_{LU}}{A_{LU}} \sim -0.001$.

likelihood function can be obtained [11, 12]:

$$L(\mathbf{x}) = L^{\rightarrow}(\mathbf{x})L^{\leftarrow}(\mathbf{x}), \quad (36)$$

$$L^{\rightleftharpoons}(\mathbf{x}) = \prod_{i=1}^{N^{\rightleftharpoons}} \frac{1 \pm P^{\rightleftharpoons} A_{LU}(\phi_i^{\rightleftharpoons}; \mathbf{x})}{C^{\rightleftharpoons}(\mathbf{x})}, \quad (37)$$

$$C^{\rightleftharpoons}(\mathbf{x}) = \frac{\sum_{i=1}^{N^{\rightarrow}} 1 \pm P^{\rightarrow} A_{LU}(\phi_i^{\rightarrow}; \mathbf{x})}{P^{\rightarrow} N_{DIS}^{\rightarrow}} + \frac{\sum_{i=1}^{N^{\leftarrow}} 1 \pm P^{\leftarrow} A_{LU}(\phi_i^{\leftarrow}; \mathbf{x})}{P^{\leftarrow} N_{DIS}^{\leftarrow}}, \quad (38)$$

where $A_{LU}(\phi_i; \mathbf{x}) = A_{LU}^{\sin \phi} \sin \phi_i + A_{LU}^{\sin 2\phi} \sin 2\phi_i$.

The BSAs can then be extracted by the maximum likelihood fit.

3 Results and Conclusion

3.1 Data Statistics

The average beam polarizations, event numbers, and the average kinematics of the exclusive events are summarized in Table 1.

	00d0 unpol. e^+		05b1 un.+pol. e^-	
	\rightarrow	\leftarrow	\rightarrow	\leftarrow
$\langle P \rangle (\%)$	54.3	55.1	32.4	28.6
N_{DIS}	1,878,128	3,214,467	2,344,492	1,275,040
N	2,801	4,983	3,661	2,081
$\langle -t_c \rangle (GeV^2)$	0.12		0.12	
$\langle x_{Bj} \rangle$	0.10		0.09	
$\langle Q^2 \rangle (GeV^2)$	2.5		2.4	
$\langle y \rangle$	0.51		0.51	

Table 1: Summary for the average beam polarizations, event numbers, and the average kinematics of the exclusive events.

3.2 BSAs with e^{\pm} Beams

The results by the least square fit are shown in Figure 8.

The binning will introduce an additional limitation on the resolution of ϕ , resulting in a loss of information and hence larger statistical errors for the parameter estimates especially with low statistics. The maximum likelihood method does not depend on the binning and is more reliable [11, 12]. Therefore in this report, results shown are obtained by the method of maximum likelihood (Table 2, Figure 9).

Within statistical uncertainties, the magnitudes of the BSAs with e^{\pm} beams are compatible.

beam	$A_{LU}^{\sin\phi} \pm (stat.)$	$A_{LU}^{\sin 2\phi} \pm (stat.)$
e^+	-0.17 ± 0.03	-0.01 ± 0.03
e^-	0.26 ± 0.06	0.06 ± 0.06

Table 2: Results on BSAs for two different beam charges, obtained by the method of maximum likelihood.

3.3 Kinematic Dependence of the BSAs with e^\pm Beams

The kinematic dependence of the BSAs with e^\pm beams is shown in Figure 10. In different kinematic bins, similar results to the ones in Section 3.2 are obtained, i.e., within statistical uncertainties, $-A_{LU}^{\sin\phi, e^+} \simeq A_{LU}^{\sin\phi, e^-}$ is observed over all variables.

3.4 Conclusion

In this analysis, beam spin asymmetries were extracted for both beam charges, using the HERMES data productions. Systematic studies were not performed yet, hence the uncertainties given in this report are statistical only. Within statistical uncertainties, the magnitudes of the BSAs with e^\pm beams are compatible. These results agree with the theoretical predictions.

Acknowledgments

This work is partly supported by the President Fund at Peking University and the DESY Summer School Program. It is finished with the important help of Zhenyu Ye. Caroline Riedl and Hayg Guler also helped to solve some critical problems. Wolf-Dieter Nowak gave many important comments on the manuscript.

References

- [1] A.V. Belitsky, D. Müller, A. Kirchner, Nucl. Phys. B 629 (2002) 323-392.
- [2] X. Ji, Phys. Rev. D 55 (1997) 7114.
- [3] X. Ji, Phys. Rev. Lett. 78 (1997) 610.
- [4] K. Ackerstaff et al., HERMES Collaboration, arXiv:hep-ex/9806008.
- [5] J.D. Jackson, Reviews of Modern Physics, Vol. 48, No.3, July 1976.
- [6] F. Ellinghaus, J. Volmer, Beam-Spin Asymmetry from Deeply Virtual Compton Scattering on Neon and Deuterium. HERMES Release Report, 2002.
- [7] F. Ellinghaus, Beam-Charge and Beam-Spin Azimuthal Asymmetries in Deeply-Virtual Compton Scattering, HERMES Doctoral Thesis, 2003.

- [8] Z. Ye, et al., Transverse Target-Spin Asymmetry in Deeply Virtual Compton Scattering on the Proton. HERMES Release Report, 2005.
- [9] B. Krauss, Deeply Virtual Compton Scattering and the HERMES-Recoil-Detector, HERMES Doctoral Thesis, 2005.
- [10] S. Haan, Deeply Virtual Compton Scattering on Neon, HERMES Diploma Thesis, 2005.
- [11] A. Miller, presentations, 2005-2006.
- [12] Z. Ye, private communication.

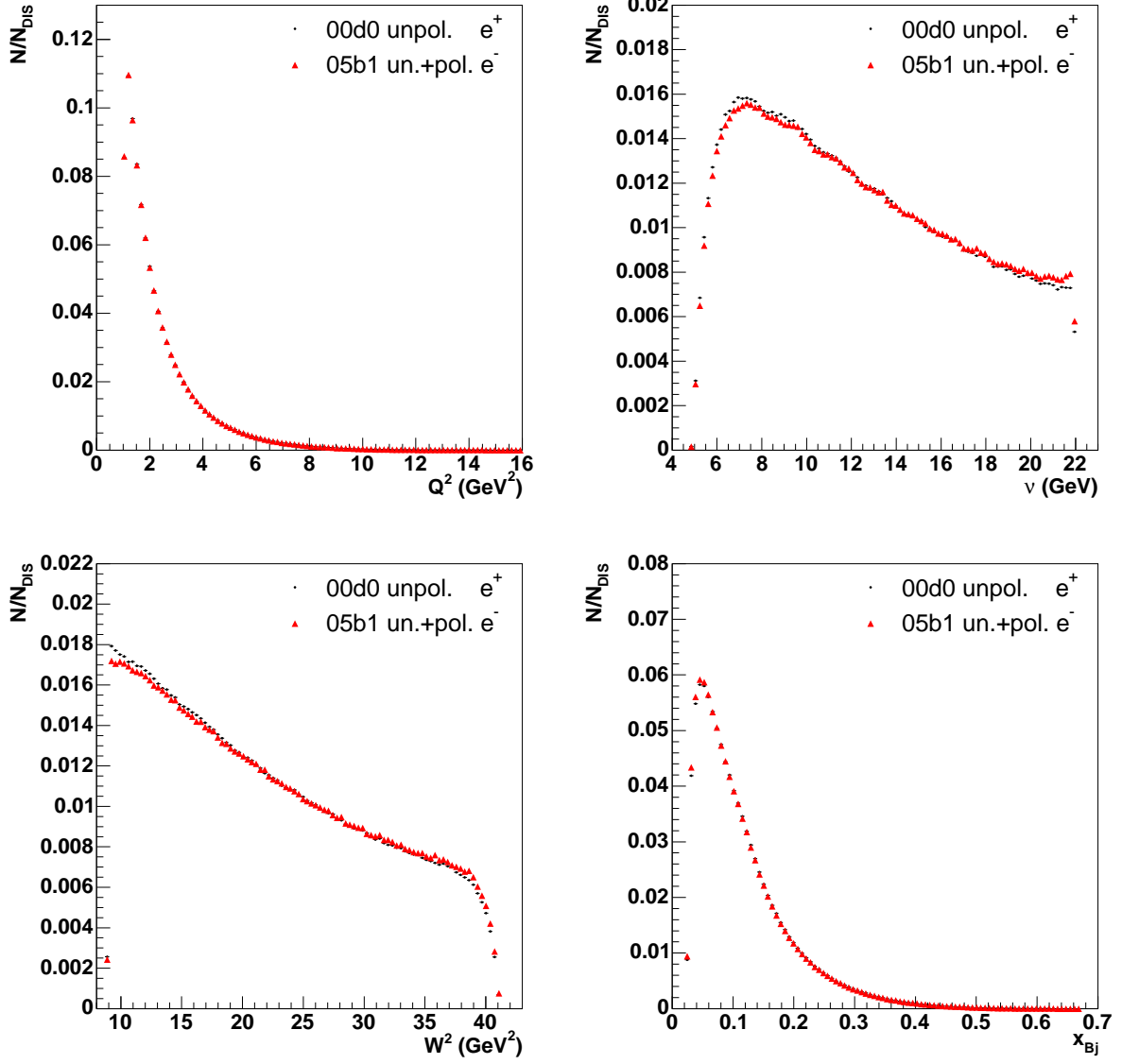


Figure 4: Kinematic distributions of the DIS events, normalized per DIS event. At the limits of ν and W^2 , differences between the distributions from the two data productions are pronounced. $N_{DIS}^{00d0, \text{unpol.}} = 5,092,595$, $N_{DIS}^{05b1, \text{pol.} + \text{unpol.}} = 3,619,532$.

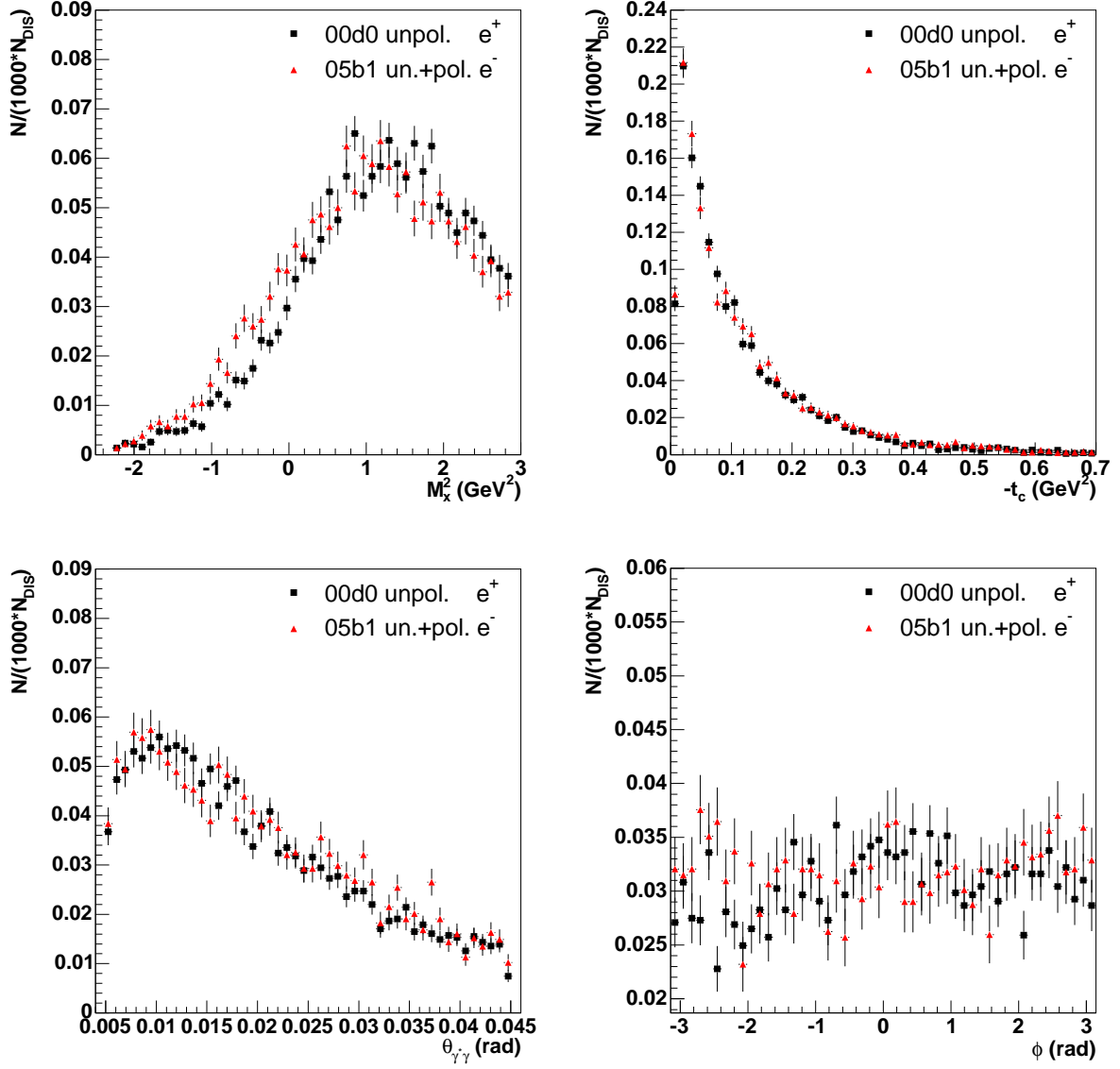


Figure 5: Kinematic distributions of the exclusive events, normalized per 1000 DIS events.
 $N_{\text{Exclusive}}^{00d0, \text{unpol.}} = 7,784$, $N_{\text{Exclusive}}^{05b1, \text{pol.} + \text{unpol.}} = 5,742$.

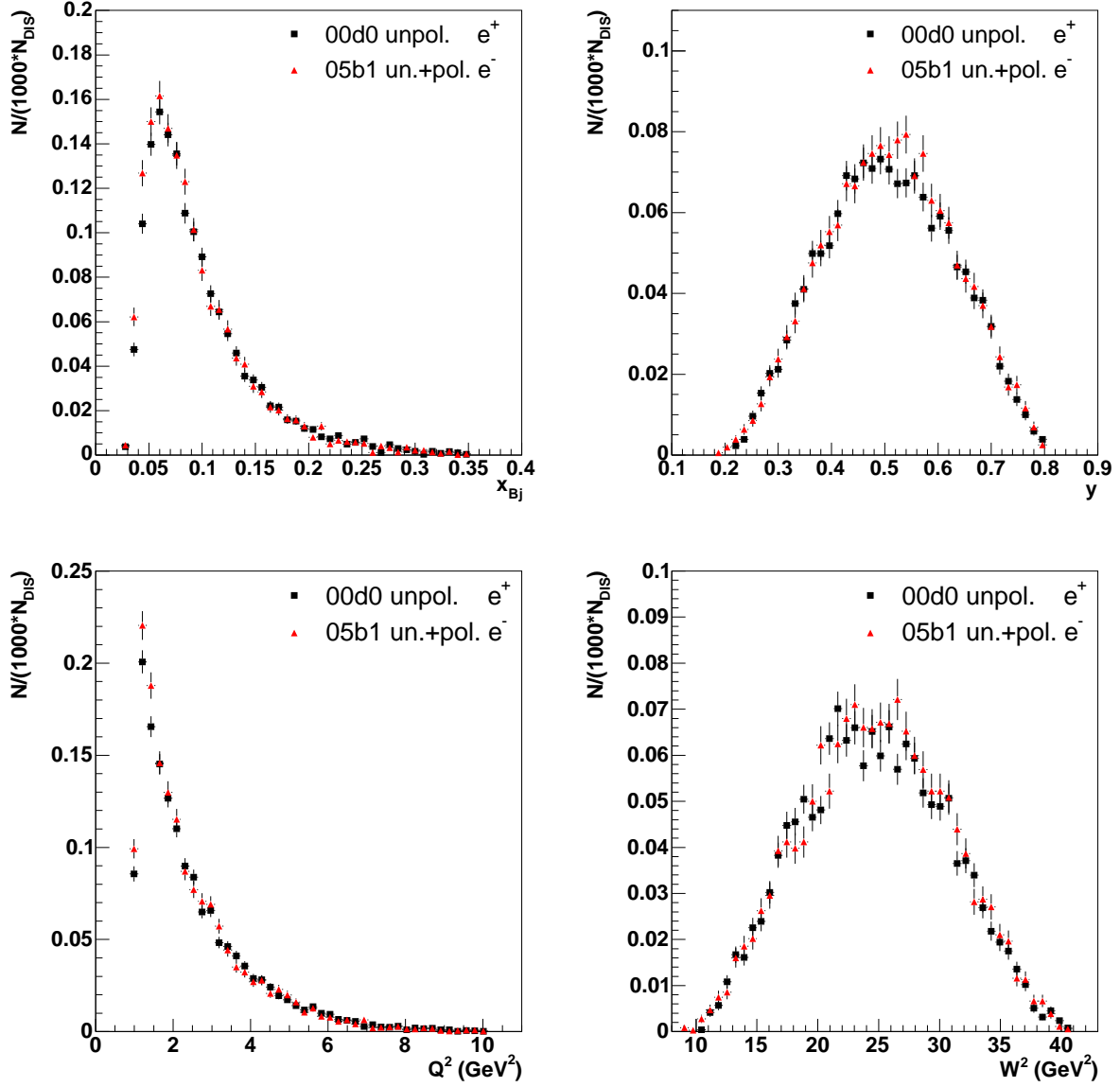


Figure 6: Kinematic distributions of the exclusive events, normalized per 1000 DIS events. The average values for the 00d0/05b1 production are: $\langle x_{Bj} \rangle = 0.10 / 0.09$, $\langle y \rangle = 0.51 / 0.51$, $\langle Q^2 \rangle = 2.5 / 2.4 \text{ GeV}^2$, $\langle W^2 \rangle = 24.6 / 24.8 \text{ GeV}^2$.

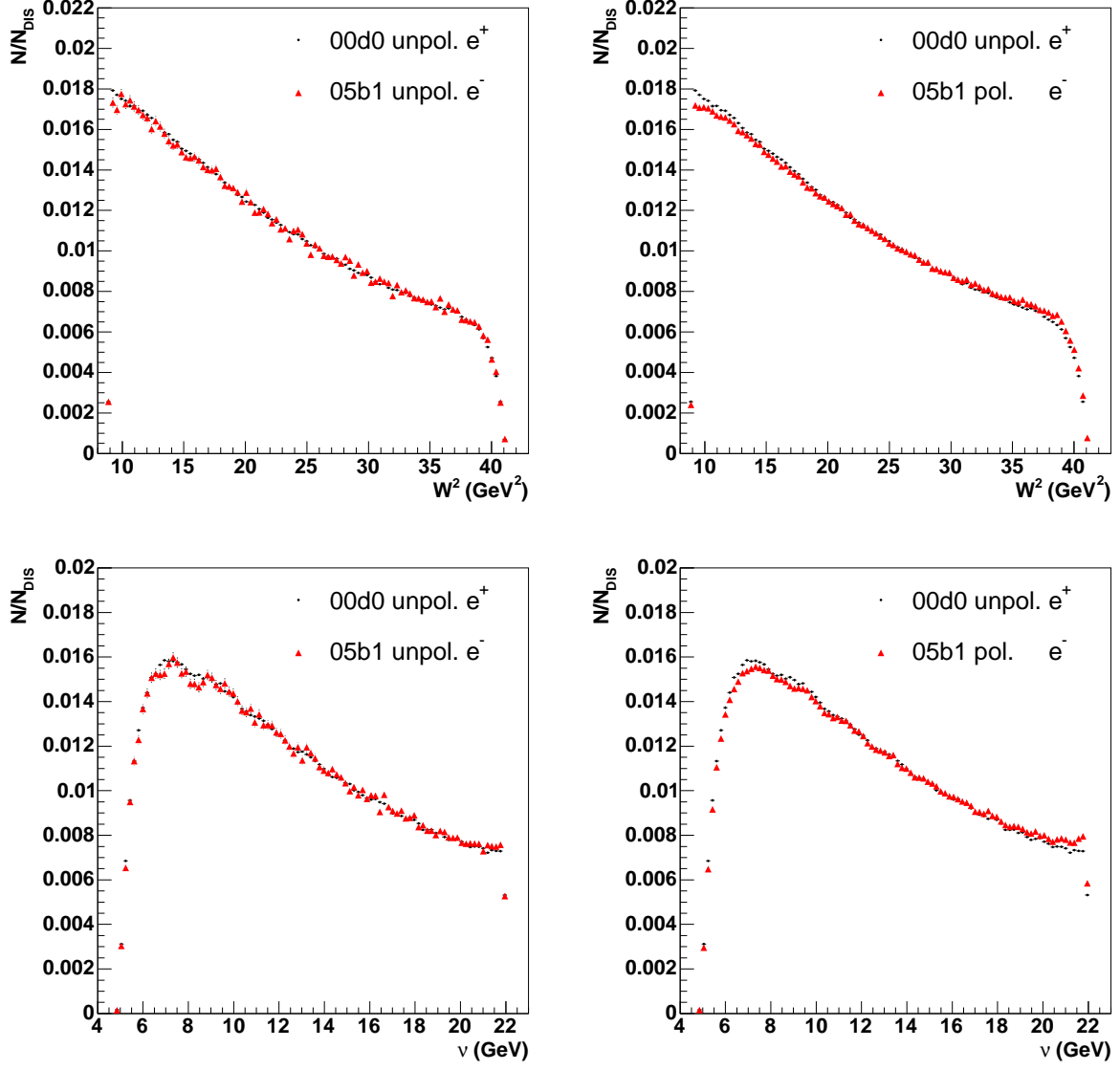


Figure 7: Kinematic distributions of the DIS events, normalized per DIS event. For the distributions from the 00d0 unpolarized and 05b1 polarized data, greater differences are observed at kinematic limits.

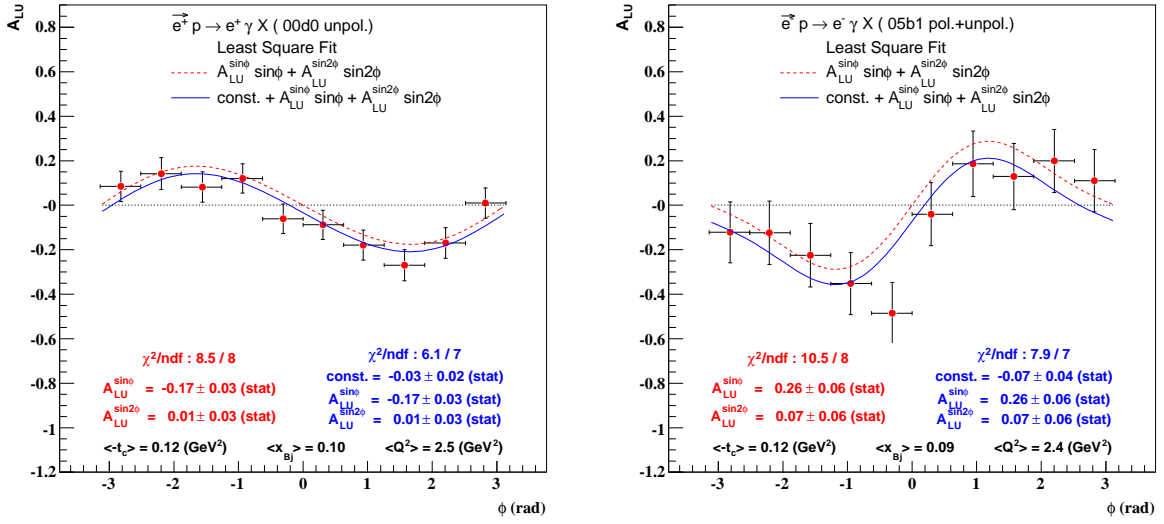


Figure 8: BSAs with e^\pm beams by the least square fit to different functions. The results indicate that whether the fitting function has a constant term does not have critical influence on the extraction of $A_{LU}^{\sin\phi}$ and $A_{LU}^{\sin 2\phi}$.

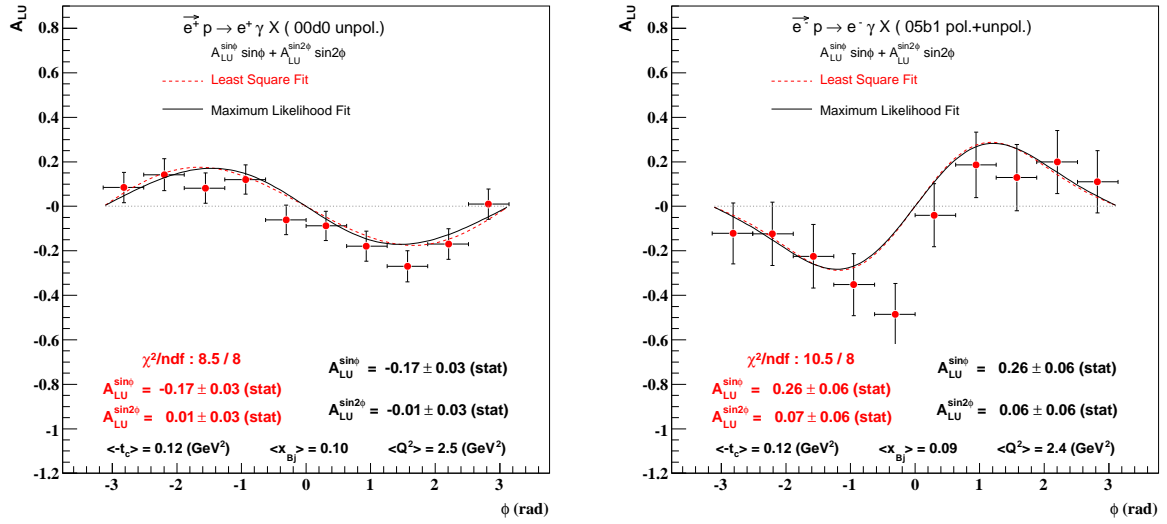


Figure 9: BSAs with e^\pm beams by different fits to a function without constant term. Results by different methods are compatible. The points calculated by Eqs. (32) and (33) and the dash lines by the least square fit to the points are for the comparison with the adopted results by the unbinned maximum likelihood method (solid lines).

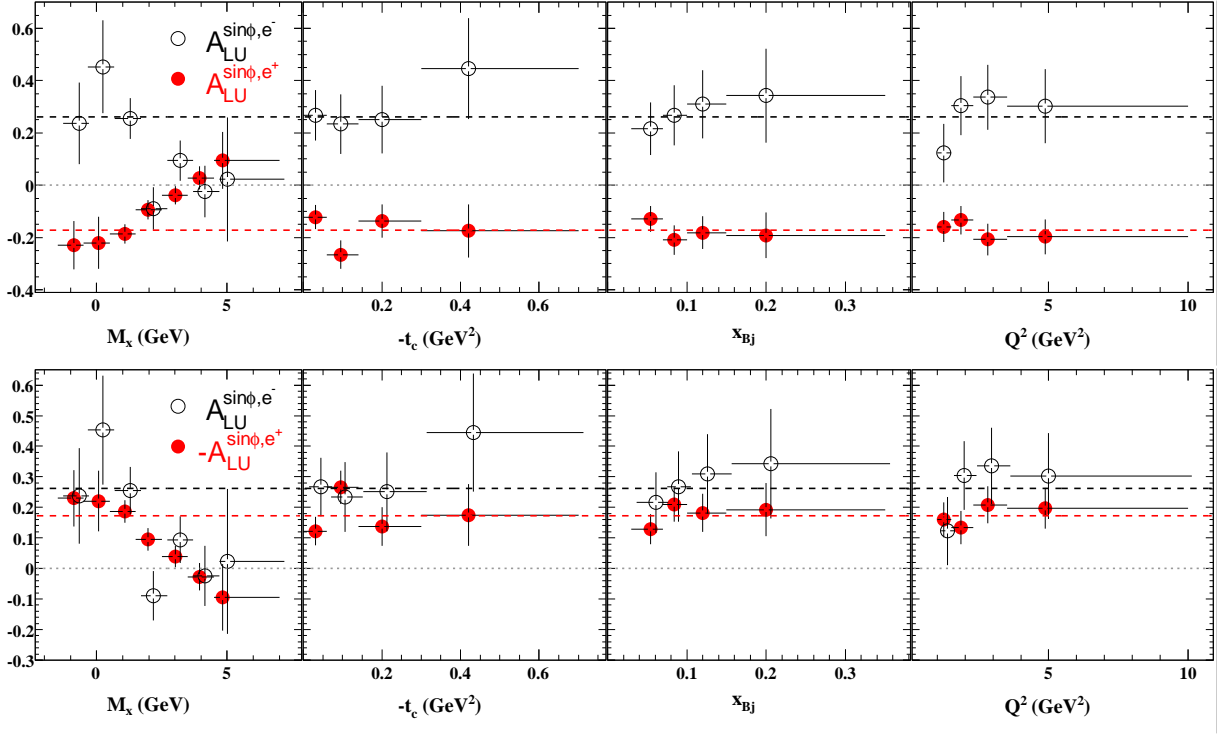


Figure 10: Kinematic dependence of the BSAs with e^\pm beams. The BSAs with an e^+ beam in the bottom figure is scaled by -1. The black and red dashed lines correspond to the average results with e^- and e^+ beams respectively.